Sequence-Based Control of an Isolated DC/AC Matrix Converter

Alireza Tajfar, *Student Member, IEEE*, and Sudip K. Mazumder, *Senior Member, IEEE*

***Abstract*—This paper describes the control of an isolated multiphase high-frequency-link (HFL) matrix inverter by controlling the time evolution of its switching states (or, switching sequences). It is referred to as the optimal-switching-sequence-based control (OSBC). Unlike several conventional control schemes, where, typically the control is based on averaged model of the inverter and the modulation scheme sets a predetermined switching sequence, OSBC synthesizes the fundamental switching sequence depending on the control needs on the fly. For instance, OSBC can seamlessly play with the inverter switching sequences if the input voltage of the inverter changes as evident in solar or wind-based energy systems. This necessitates that OSBC use a switching-sequence-based discontinuous (instead of averaged) modeling approach. Further, the stability of the closed-loop inverter is determined in OSBC using an advanced composite Lyapunov-function based approach, which also enables one to predetermine the reachability of the inverter dynamics for a given switching sequence. Thus, optimal control in OSBC is ensured under stability bound of the switching sequence. This provides a fundamental difference between OSBC and model predictive control for inverters. This also implies that in a multiobjective OSBC, one can shift the weights of the individual cost functions to yield better inverter performance without compromising the stability.**

***Index Terms*—Capacitor-less dc-link, control, inverter, Lyapunov function, map, matrix converter, modeling, optimal, renewable/alternative energy, stability, switching sequence, three phase.**

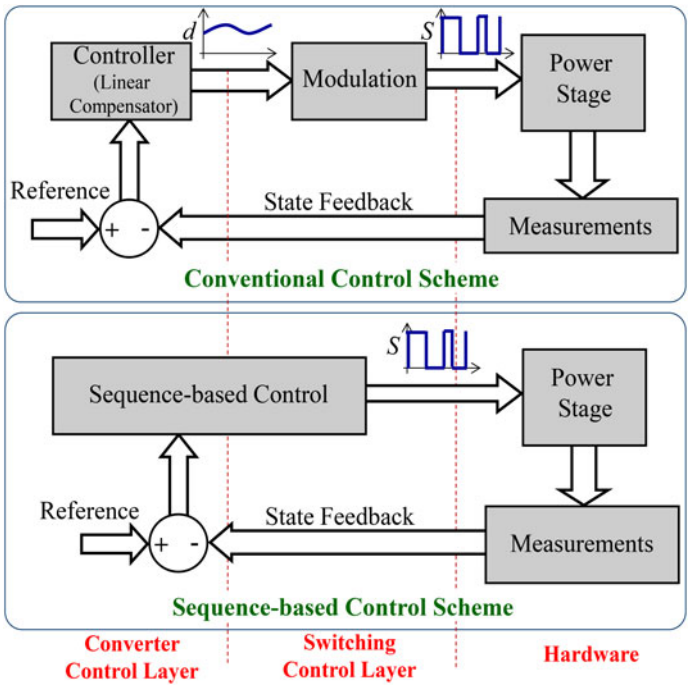

Fig. 1. Block diagram illustrating a comparison between a conventional control scheme for power electronic converters and a sequence-based control scheme.

I. Introduction

HIGH-FREQUENCY-LINK (HFL) power-conversion systems (PCSs) have been widely studied recently as a popular interface between renewable energy sources and loads/utility grid [1], [2]. Among various proposed topologies, the capacitor-less isolated dc/ac matrix converter or HFL inverter has gained tremendous significance in recent years due to its superior benefits of cost, modular design and scalability, high power density, efficiency, and fault-tolerant operability [1]–[11]. However, removal of a bulky dc-link capacitor leads to the following challenges:

1) lack of an intermediate buffer stage between different power stages of the HFL inverter results in interference between control actions implemented in different stages;
2) stiffness of the HFL inverter is reduced against source/load transients since there is no temporary power storage such as a bulky dc-link capacitor.

Hence, in order to take the full advantage of this perfect topology for renewable energy applications, the aforementioned issues need to be addressed properly. Regarding the first issue, the potential solution to implement different control objectives effectively and without interference in such a buffer-less multistage topology seems to be an optimization-oriented algorithm. To address the second issue, one possible solution is to design a high bandwidth power conversion to provide fast enough dynamic response for the power stage. However, this requires a high switching frequency, which also increases the switching losses and degrades the efficiency of the HFL inverter [11]. Yet another approach is to control the time evolution of the switching states (i.e., the switching sequence) of the inverter in such a way so that optimal dynamic response is achieved for

Manuscript received October 11, 2014; revised January 2, 2015 and March 7, 2015; accepted April 7, 2015. Date of publication April 22, 2015; date of current version September 29, 2015. The work of S. K. Mazumder was supported in part by the U.S. National Science Foundation (NSF) Award (Nos. 0725887, 0239131, and 1239118). However, any opinions, findings, conclusions, or recommendations expressed herein are those of the authors and do not necessarily reflect the views of the NSF. Recommended for publication by Associate Editor M. Saeedifard.

A. Tajfar is with the Enphase Energy, Petaluma, CA 94954 USA (e-mail: alirezat4u@gmail.com).

S. K. Mazumder is with University of Illinois at Chicago, Chicago, IL 60607 USA (e-mail: mazumder@uic.edu).

Color versions of one or more of the figures in this paper are available online at http://ieeexplore.ieee.org.

Digital Object Identifier 10.1109/TPEL.2015.2425732

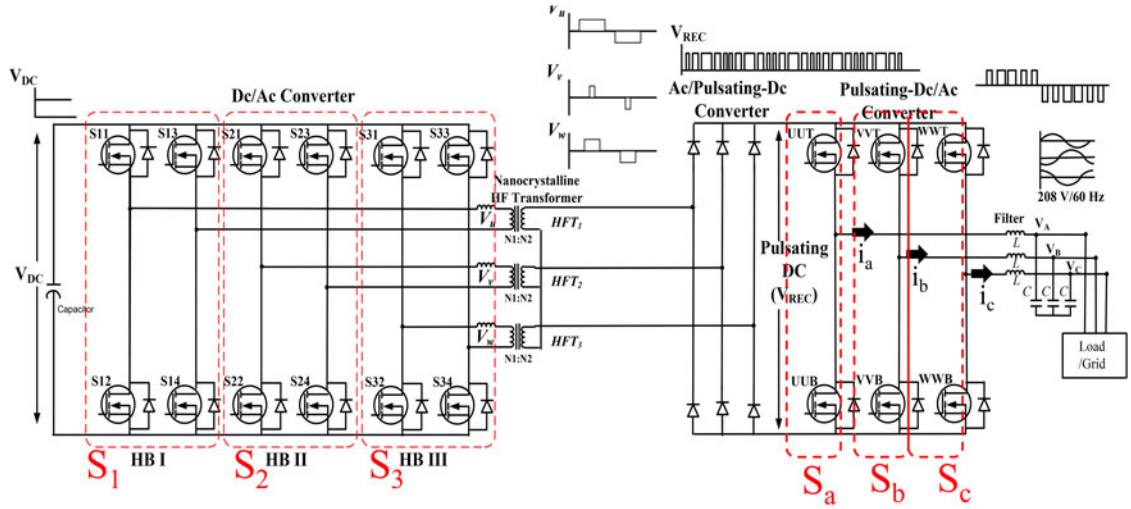

Fig. 2. Topology and definition of switching functions (*S*1, *S*2, *S*3, *Sa*, *Sb*, and *Sc*) of the isolated dc/ac matrix converter (i.e., HFL inverter).

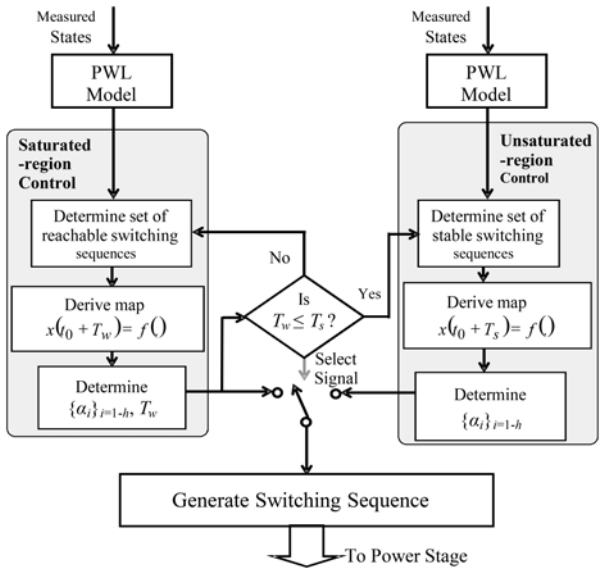

Fig. 3. Schematic illustrating the operation of OSBC. The "Select Signal" is used to switch from SROC to USROC when $T_w < T_s$.

a given switching frequency. The traditional control of the inverter in synchronous or stationary frame implement the basic control scheme without the modulator under consideration, and then, use a predetermined modulation scheme to transform the continuous output of the controller to a discontinuous one that after level shifting can be used to activate the devices of the inverter [12]. The reason behind such a two-step implementation is that, typically the averaged output of the inverter evolves on a slow scale (e.g., 60/50-Hz scale) and the fast scale is essentially filtered. Recently, authors have demonstrated that by directly controlling the sequence of a power converter, control and modulation can be integrated, as illustrated in Fig. 1 [13], [14], [17], and [18]. Such a closed-loop controller does not need a predefined modulation scheme, and hence, the switching sequence can be generated on the fly simply based on a single or multiobjective cost function. The HFL inverter shown in Fig. 2 is used to show the effectiveness of the proposed controller. We will demonstrate in Section III, the superior transient performance of this optimal-sequence-based control (OSBC). What is unique about this OSBC, as described in this paper, the control is achieved under stability bound. That is even though the inverter has multiple but finite switching sequences, a unique multiple Lyapunov-function-based stability approach [14] (as outlined in Section II) determines which of these switching sequence ensures reachability and these feasible sequences are used for OSBC under stability bound. OSBC thus is different from the traditional model-predictive control and sliding-mode control [16]. Moreover, since OSBC is implemented through solving an optimal problem, joint optimization of various control objectives (which could happen at different scales) such as voltage regulation (VR) in standalone mode of operation, grid control (GC) in grid-connected mode of operation, switching-loss mitigation and maximum power point tracking (MPPT) could be realized. Joint optimization of such multiscale parameters are also developed and verified through several results in this paper.

II. OSBC

OSBC is an advanced model predictive control that directly controls the evolution of switching states (switching sequences) of devices (such as MOSFETs) in a power converter through minimization of a predefined cost function. As a result, the optimal switching sequences and also the relevant time horizon for which the HFL inverter stays in each switching state are determined. A flowchart for OSBC is shown in Fig. 3, which shows that the overall control comprises two key elements: (a) a saturated-region optimal control (SROC) that controls the converter dynamics from an arbitrary initial condition to the steady-state or orbit using reachable or converging switching sequence(s); and (b) an unsaturated-region optimal control (USROC) that controls the steady-state dynamics of the converter (i.e., using switching sequence that ensures periodic orbital stability). In this section, the necessary steps for development of the OSBC scheme for a three-phase HFL inverter are described

in detail. The first step is to derive a piecewise-linear (PWL) model for the HFL inverter in terms of switching functions defined according to the number of switching devices and their modes of operation in the HFL inverter. Having set the PWL model, first the total number of possible switching sequences is determined, and then, a set of reachable/feasible switching sequences is selected based on a reaching criterion described in this paper. The final step is to design an OSBC scheme that is a constrained optimization problem aimed to minimize a predetermined cost function under system constraints.

A. General PWL Modeling of an Isolated Three-Phase HFL Inverter (Standalone Operation)

With respect to Fig. 2, showing the topology of an HFL inverter, three switching functions are defined, respectively, for three legs in the pulsating-dc/ac converter as S_a, S_b, and S_c such that $S_a, S_b, S_c \in \{0, 1\}$ (top and bottom switches in each leg switch complementary to avoid a short circuit in the input dc source). For instance, $S_a = 1$ is equivalent to (UUT $= 1$ and UUB $= 0$) and vice versa. Also, for each H-bridge in the front-end dc/ac converter (HBI, HBII, and HBIII), a switching function is associated such that $S_1, S_2, S_3 \in \{-1, 0, 1\}$ (depending on whether the polarity of the bipolar and tristate pulse train generated is negative, zero, or positive). As such, $S_1 = 1$ indicates ($S_{11} = S_{14} = 1$ and $S_{12} = S_{13} = 0$), $S_1 = -1$ indicates ($S_{11} = S_{14} = 0$ and $S_{12} = S_{13} = 1$), and $S_1 = 0$ indicates ($S_{11} = S_{13} = 1$ and $S_{12} = S_{14} = 0$) or ($S_{11} = S_{13} = 0$ and $S_{12} = S_{14} = 1$). However, since ac/pulsating-dc Converter rectifies the pulse train outputs of three HF transformers, the values of 1 and -1 could be treated the same while tabulating the switching state table.

The state vector for this HFL inverter is defined as $x = (i_a, i_b, i_c, v_a, v_b, v_c)^T$ consisting of the HFL inverter three-phase output currents and voltages. A PWL state-space model is derived for the HFL inverter which is of the form

$$\dot{x} = Ax + B_{i,j} \tag{1}$$

where i represents the switching sequence of the HFL inverter, j determines the switching states of the ith switching sequence, x represents the converter states, and A and $B_{i,j}$ are matrices and vectors of appropriate dimensions that model the converter in each switching state. First, a set of differential equations in terms of states and switching functions are written for the HFL inverter using the KVL and KCL as follows:

$$\begin{cases} L\frac{d}{dt}\dot{i}_{abc} = \frac{1}{3}B'S_{abc}V_{\text{REC}} - V_{abc} \\ C\frac{d}{dt}V_{abc} = i_{abc} - \frac{1}{R}V_{abc} \end{cases} \tag{2}$$

where $i_{abc} = (i_a, i_b, i_c)^T$, $V_{abc} = (v_a, v_b, v_c)^T$, $S_{abc} = (S_a, S_b, S_c)^T$, $V_{\text{REC}} = \frac{N_2}{N_1}V_{\text{DC}}\max(S_1 - S_2, S_1 - S_3, S_2 - S_3)$, and $B' = [2, -1, -1; -1, 2, -1; -1, -1, 2]$. Based on the aforementioned set of differential equations, a PWL model for the HFL inverter in terms of switching functions and in the stationary abc frame is derived as follows:

$$\dot{X}_{abc} = A_{abc}X_{abc} + B_{abc}$$

$$A_{abc} = \begin{bmatrix} 0 & 0 & 0 & -\frac{1}{L} & 0 & 0 \\ 0 & 0 & 0 & 0 & -\frac{1}{L} & 0 \\ 0 & 0 & 0 & 0 & 0 & -\frac{1}{L} \\ \frac{1}{C} & 0 & 0 & -\frac{1}{\text{RC}} & 0 & 0 \\ 0 & \frac{1}{C} & 0 & 0 & -\frac{1}{\text{RC}} & 0 \\ 0 & 0 & \frac{1}{C} & 0 & 0 & -\frac{1}{\text{RC}} \end{bmatrix}$$

$$B_{abc} = \frac{V_{\text{REC}}}{3L} \times B' \times \bar{S}_{abc}, \bar{S}_{abc} = [S_a, S_b, S_c]^T \tag{3}$$

and $X_{abc} = (i_a, i_b, i_c, v_a, v_b, v_c)^T$. However, in order to make the controller design more straightforward and to deal with dc variables instead of ac ones, the PWL model in (3) is mapped into synchronous (*dq*) frame using Park's transformation [12] to yield

$$\dot{\bar{X}}_{dq} = A_{dq}\bar{X}_{dq} + B_{dq}$$

$$A_{dq} = \begin{bmatrix} T & 0_{3\times3} \\ 0_{3\times3} & T \end{bmatrix} \times A_{abc} \times \begin{bmatrix} T^{-1} & 0_{3\times3} \\ 0_{3\times3} & T^{-1} \end{bmatrix}$$

$$= \begin{bmatrix} 0 & \omega & -1/L & 0 \\ -\omega & 0 & 0 & -1/L \\ 1/C & 0 & -1/RC & \omega \\ 0 & 1/C & -\omega & -1/RC \end{bmatrix}$$

$$B_{dq} = \begin{bmatrix} T & 0_{3\times3} \\ 0_{3\times3} & T \end{bmatrix} \times B_{abc} = \begin{bmatrix} S_d \\ S_q \\ 0 \\ 0 \end{bmatrix} \times \frac{V_{\text{REC}}}{L} \tag{4}$$

where T is the Park's transformation matrix, $X_{dq} = (i_d, i_q, v_d, v_q)^T$, ω is the line (slow scale) angular frequency, and S_d and S_q are the switching functions in *dq* frame. Note that B_{abc} and B_{dq} are functions of switching sequences as stated in the general form (1). The total number of switching states base on the mapped switching functions S_d and S_q as well as S_{d1} and S_{q1} (equivalents of S_1, S_2, and S_3 in *dq* reference frame) are provided in Table I.

Based on the possible switching states mentioned in Table I, the total number of feasible combinations of switching sequences is obtained as follows [14]:

$$M = \sum_{l=1}^{(2^N - W)} \left(\frac{(2^N - W)!}{l!\,(2^N - W - l)!} \right)$$

$$= \sum_{l=1}^{(2^4)} \left(\frac{(2^4 - 0)!}{l!\,(2^4 - l)!} \right) = 65\,535 \tag{5}$$

where *N* is the total number of noncomplementary switching functions and *W* is the number of redundant switching states (switching states for which the state-space equations of the

TABLE I
POSSIBLE SWITCHING STATES FOR THE HFL INVERTER

I	S_d	S_q	S_{d1}	S_{q1}
1	0	0	0	0
2	0	0	0	1
3	0	0	1	0
4	0	0	1	1
5	0	1	0	0
6	0	1	0	1
7	0	1	1	0
8	0	1	1	1
9	1	0	0	0
10	1	0	0	1
11	1	0	1	0
12	1	0	1	1
13	1	1	0	0
14	1	1	0	1
15	1	1	1	0
16	1	1	1	1

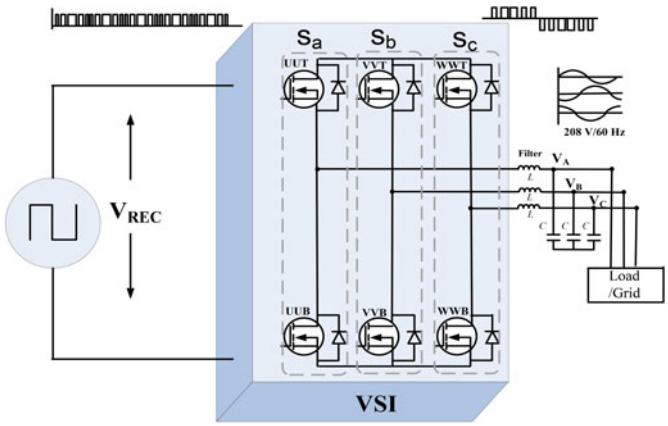

Fig. 4. Simplified topology of HFL inverter used for PWL modeling with reduced number of switching functions.

switching system are identical such as switching states resulting in a zero-voltage level for a full bridge). With a search space of this size, the optimization process will take so long since the OSBC algorithm needs to search for the optimal switching sequence among a total number of 65 535 feasible candidates. Therefore, in order to reduce the search space and increase the rate of optimization, a modified modeling approach is chosen, which is explained next.

B. Modified PWL Modeling of an Isolated Three-Phase HFL inverter (Standalone Operation)

As stated in the previous section, in order to reduce the search space and to speed up the optimization process, a modified model of the HFL inverter will be derived. The HFL inverter of Fig. 2 could be considered as a standard voltage-source inverter (VSI) connected to a pulsating-dc voltage source input, $V_{\rm REC}$ (see Fig. 4). As shown in (4), $V_{\rm REC}$ is embedded in B_{dq}. In order to modify the PWL model (4) of the HFL inverter, first a Fourier series representation of $V_{\rm REC}$ is considered as follows:

$$V_{\rm REC} = \frac{1}{2}a_0 + \sum_{n=1}^{\infty}\{a_n \cos\omega_n t + b_n \sin\omega_n t\} \tag{6}$$

where $a_0 = \langle V_{\rm REC}\rangle$, $a_n = \frac{\sin(2n\pi D)}{n\pi}V_{\rm REC}$, $b_n = \frac{V_{\rm REC}}{n\pi}\{1-\cos(2n\pi D)\}$, $\omega_n = 2n\pi/T_p$, represents the frequency of the *n*th-order harmonic component of $V_{\rm REC}$ (T_p is the period of the fundamental component of $V_{\rm REC}$), and D is the duty cycle of pulses in $V_{\rm REC}$. Incorporating the Fourier series expansion of $V_{\rm REC}$ (6) in (4), an augmented PWL model of the HFL inverter could be derived. First, for each frequency component of $V_{\rm REC}$, two additional states y_{n1} and y_{n2} are defined as follows:

$$y_{n1} = a_n \cos\omega_n t + b_n \sin\omega_n t \tag{7a}$$

$$\frac{dy_{n1}}{dt} = -\omega_n a_n \sin\omega_n t + \omega_n b_n \cos\omega_n t = y_{n2} \tag{7b}$$

$$\frac{dy_{n2}}{dt} = -\omega_n^2 a_n \cos\omega_n t - \omega_n^2 b_n \sin\omega_n t = -\omega_n^2 y_{n1}. \tag{7c}$$

An augmented PWL model for the HFL inverter using the simplified model in Fig. 4 is derived as follows:

$$\frac{d}{dt}\begin{bmatrix} X^{dqz} \\ y_{11} \\ y_{12} \\ \vdots \\ y_{n1} \\ y_{n2} \end{bmatrix} = \begin{bmatrix} A_{4\times4}^{dqz} & B_{4\times1}^{dqz} & 0_{4\times1} & & B_{4\times1}^{dqz} & 0_{4\times1} \\ 0_{1\times4} & 0 & 1 & \cdots & 0 & 0 \\ 0_{1\times4} & -\omega_1^2 & 0 & & 0 & 0 \\ & \vdots & & \ddots & \vdots & \\ 0_{1\times4} & 0 & 0 & \cdots & 0 & 1 \\ 0_{1\times4} & 0 & 0 & & -\omega_n^2 & 0 \end{bmatrix} \times \begin{bmatrix} X^{dqz} \\ y_{11} \\ y_{12} \\ \vdots \\ y_{n1} \\ y_{n2} \end{bmatrix} + \begin{bmatrix} B_{4\times1}^{dqz} \\ 0 \\ 0 \\ \vdots \\ 0 \\ 0 \end{bmatrix} \times \frac{a_0}{2}. \tag{7d}$$

C. Modified PWL Modeling of an Isolated Three-Phase HFL Inverter (Grid-Connected Operation)

Thus, far a discontinuous model in terms of switching functions was derived for standalone operation. For grid-connected operation, the state vector in *abc* synchronous reference frame and *dq* stationary reference frame would be $X_{abc} = (i_a, i_b, i_c, V_{\rm DC})^T$ and $X_{dq} = (i_d, i_q, V_{\rm DC})^T$, respectively. Input vector "*U*" in the general form of $\dot{x}(t) = Ax(t) + BU$ is $U = [-V_{gd}, -V_{gq}, i_{\rm pv}]^T$, where $i_{\rm pv}$ is the output current of a photovoltaic (PV) panel. According to the KVL and assuming a symmetrical three-phase system, we have the following set of

differential equations:

$$\overline{V_g}_{abc} = -R_{\text{line}}\bar{i}_{abc} - L\dot{\bar{i}}_{abc} + \frac{1}{3}B' \times \bar{S}_{abc}.V_{\text{REC}} \quad (8)$$

$$C\dot{V}_{\text{DC}} + \bar{S}_{abc}.\bar{i}_{abc} \times \text{MAX}\left(|S_1 - S_2|, |S_1 - S_3|, |S_2 - S_3|\right) = i_{\text{pv}} \quad (9)$$

where R_{line} is the equivalent total resistance of the output filter and engage cables connecting the inverter to the grid. As stated before, different terms included in the aforementioned equations are $\bar{i}_{abc} = (i_a, i_b, i_c)^T$, $\overline{V_g}_{abc} = (v_a, v_b, v_c)^T$, $\bar{S}_{abc} = (S_a, S_b, S_c)^T$, $V_{\text{REC}} = \frac{N_2}{N_1} \times V_{\text{DC}} \times \text{MAX}\{(S_1 - S_2), (S_1 - S_3), (S_2 - S_3)\}$, and B' is defined earlier. In order to simplify (8) and (9), we assume that in the front-end dc/ac converter only two full bridges operate (those with switching functions S_1 and S_2) and the third one is a redundant phase for fault-tolerant operation [15]. Therefore, we have the followings:

$$C\dot{V}_{\text{DC}} + \bar{S}_{abc}.\bar{i}_{abc} \times (|S_1 - S_2|) = i_{\text{pv}} \quad (10)$$

$$V_{\text{REC}} = \frac{N_2}{N_1} \times V_{\text{DC}} \times (S_1 - S_2). \quad (11)$$

Using (1), (8), (10), and (11), matrices A_{abc} and B_{abc} for the PWL model of the HFL inverter in grid-connected operation are derived in *abc* stationary reference frame as follows: (12) as shown bottom of the next page.

Using the Park transformation matrix, the mathematical model of an HFL inverter in *dq* rotating frame can be derived as follows:

$$L\dot{\bar{i}}_{dq} + R\dot{\bar{i}}_{dq} + f(\omega).L.\dot{\bar{i}}_{dq} = (S_1 - S_2).N.V_{\text{DC}}.\bar{S}_{dq} - \bar{V}_{gdq} \quad (13)$$

$$C\dot{V}_{\text{DC}} = -\frac{3}{2}\bar{i}_{dq}.\bar{S}_{dq}(S_1 - S_2) + i_{\text{pv}} \quad (14)$$

where $f(\omega) = \begin{bmatrix} 0 & -\omega \\ \omega & 0 \end{bmatrix}$. Equations (13) and (14) lead to matrices A_{dq} and B_{dq} for the PWL model of the HFL inverter in grid-connected operation as follows:

$$A_{dq} = \begin{bmatrix} -\frac{R}{L} & \omega & N.(S_1 - S_2).S_d \\ -\omega & -\frac{R}{L} & N.(S_1 - S_2).S_q \\ \left(-\frac{3}{2}\right).\frac{(S_1 - S_2).S_d}{C} & \left(-\frac{3}{2}\right).\frac{(S_1 - S_2).S_q}{C} & 0 \end{bmatrix}$$

$$B_{dq} = \begin{bmatrix} 1/L & 0 & 0 \\ 0 & 1/L & 0 \\ 0 & 0 & 1/C \end{bmatrix}. \quad (15)$$

Discontinuous model matrices for grid-connected mode of operation could also be derived in a similar way as done for the standalone mode (using a model for VSI with pulsating-dc input source represented by a Fourier series) and are given in the following:

$$\frac{d}{dt}\begin{bmatrix} X^{dqz} \\ y_{11} \\ y_{12} \\ \vdots \\ y_{n1} \\ y_{n2} \end{bmatrix} = \begin{bmatrix} A^{dqz}_{2\times 2} & B^{dqz}_{2\times 1} & 0_{2\times 1} & & B^{dqz}_{2\times 1} & 0_{2\times 1} \\ 0_{1\times 2} & 0 & 1 & \cdots & 0 & 0 \\ 0_{1\times 2} & -\omega_1^2 & 0 & & 0 & 0 \\ & \vdots & & \ddots & \vdots & \\ 0_{1\times 2} & 0 & 0 & & 0 & 1 \\ 0_{1\times 2} & 0 & 0 & \cdots & -\omega_n^2 & 0 \end{bmatrix} \times \begin{bmatrix} X^{dqz} \\ y_{11} \\ y_{12} \\ \vdots \\ y_{n1} \\ y_{n2} \end{bmatrix} + \begin{bmatrix} B^{dqz}_{2\times 1} \\ 0 \\ 0 \\ \vdots \\ 0 \\ 0 \end{bmatrix} \times \frac{a_0}{2}. \quad (16)$$

TABLE II
POSSIBLE SWITCHING STATES FOR HFL INVERTER USING SIMPLIFIED PWL MODEL

i	S_d	S_q
1	0	0
2	0	1
3	1	0
4	1	1

Having derived these simplified discontinuous models as per Fig. 4 for either cases of standalone and grid-connected modes of operation, note that there only exist three switching functions in the HFL inverter model, i.e., S_a, S_b, and S_c in *abc* synchronous reference frame with two equivalent switching functions in *dq* stationary reference frame, i.e., S_d and S_q. Based on this, the possible switching states are given in Table II. Based on the possible switching states given in Table II, the total number of feasible combinations of switching sequences (see Table III) is obtained as follows:

$$M = \sum_{l=1}^{(2^N - W)} \left(\frac{(2^N - W)!}{l!\,(2^N - W - l)!}\right) = \sum_{l=1}^{(2^2)} \left(\frac{(2^2)!}{l!\,(2^2 - l)!}\right) = 15. \quad (17)$$

In contrast to the other optimal control methods such as model-predictive control (MPC), which has been vastly studied to control switching power converters (SPC), in OSBC only a set of reachable switching sequences are used to perform the optimal control of an SPC in general. This ensures that (as will be shown further in this paper) if control requires any jump between switching sequences, this transition would

TABLE III
POSSIBLE COMBINATIONS OF FEASIBLE SWITCHING SEQUENCES USING TABLE II

M	Switching sequences				Total number of combinations
	First switching state	Second switching state	Third switching state	Fourth switching state	
1	$i=1$				4
2	$i=2$				
3	$i=3$				
4	$i=4$				
5	$i=1$	$i=2$			6
6	$i=1$	$i=3$			
7	$i=1$	$i=4$			
8	$i=2$	$i=3$			
9	$i=2$	$i=4$			
10	$i=3$	$i=4$			
11	$i=1$	$i=2$	$i=3$		4
12	$i=1$	$i=2$	$i=4$		
13	$i=1$	$i=3$	$i=4$		
14	$i=2$	$i=3$	$i=4$		
15	$i=1$	$i=2$	$i=3$	$i=4$	1

be stable. Hence, among the total feasible switching sequences given in Table III, a reachable set is calculated using a multiple Lyapunov-function-based criteria [14] as outlined in the next section.

D. Stability Analysis of an Isolated Three-Phase HFL Inverter

In order to determine a set of reachable switching sequences among all the feasible options given in Table III, the following linear matrix inequality is solved using the simplified PWL model of the HFL inverter shown in Fig. 4:

$$\sum_{i=1}^{h} \propto_{ki} \begin{bmatrix} A^T P_{ki} + P_{ki} A & P_{ki} \bar{B}_i \\ \bar{B}_i^T P_{ki} & 0 \end{bmatrix} < 0 \qquad (18)$$

where $(k = 1, 2, \ldots, M)$, h is the number of switching states in a given switching sequence (shown in Fig. 5), $\propto_{ki}$ are the weights of the composite Lyapunov functions in each switching state such that $0 \leq \propto_{ki} \leq 1$, $\sum_{i=1}^{h} \propto_{ki} = 1$, $P_{ki} = P_{ki}^T > 0$, and $\bar{B}_i = -B_i - AX^*$. The results of reaching analysis for all of the switching sequences in Table III are shown in Fig. 6. The reaching criterion is assessed for two different modes of operation, standalone and grid connected. For the standalone mode of operation of an HFL inverter shown in Fig. 3, the simplified PWL as derived in section *B* is used for a range of a_0 between 200 and 500 V and a resistive load (P_L) varying between 2.5 and 10 kW. It is demonstrated that, the switching sequences $M = 13$ and 14 are not reachable for any input voltage dc component (a_0) and any load in the aforementioned range. Fig. 6(a) shows the result of this analysis for standalone mode of operation. For the grid-connected mode of operation, the PWL model as derived in Section II-C is used for a range of a_0 between 200 and 500 V and a range of injected active power into the grid (P_G) varying between 2.5 and 10 kW.

Note that again the switching sequences $M = 13$ and 14 are not reachable for any input voltage dc component (a_0) and any load in the aforementioned range. Fig. 6(b) shows the result of this analysis for the grid-connected mode of operation.

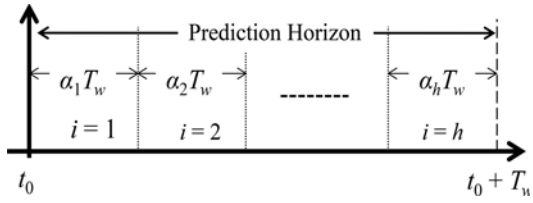

Fig. 5. Illustration of the prediction horizon for computation of the optimal control law.

E. Synthesizing an Optimal Sequence-Based Controller for an HFL Inverter

Having determined the set of reachable switching sequences, the next step is to derive a discrete map for the states of the HFL inverter over a time horizon T_w such as $X(t_0 + T_w)$, given initial values of the states $X_0 = X(t_0)$. Fig. 5 shows such a map that can be derived using a switching sequence consisting of h switching states. For USROC, the time horizon T_w is equal to the switching period. The overall map can be obtained by patching together the individual maps corresponding to each

$$A_{abc} = \begin{bmatrix} -\frac{R}{L} & 0 & 0 & & \frac{N}{L}(S_1 - S_2)(S_a - \frac{S_a+S_b+S_c}{3}) \\ 0 & -\frac{R}{L} & 0 & \ldots & \frac{N}{L}(S_1 - S_2)(S_b - \frac{S_a+S_b+S_c}{3}) \\ 0 & 0 & -\frac{R}{L} & \ldots & \frac{N}{L}(S_1 - S_2)(S_c - \frac{S_a+S_b+S_c}{3}) \\ \frac{-(S_1-S_2)S_a}{C} & \frac{-(S_1-S_2)S_b}{C} & \frac{-(S_1-S_2)S_c}{C} & & 0 \end{bmatrix}$$

$$B_{abc} = \begin{bmatrix} 1/L & 0 & 0 & 0 \\ 0 & 1/L & 0 & 0 \\ 0 & 0 & 1/L & 0 \\ 0 & 0 & 0 & 1/C \end{bmatrix}. \qquad (12)$$

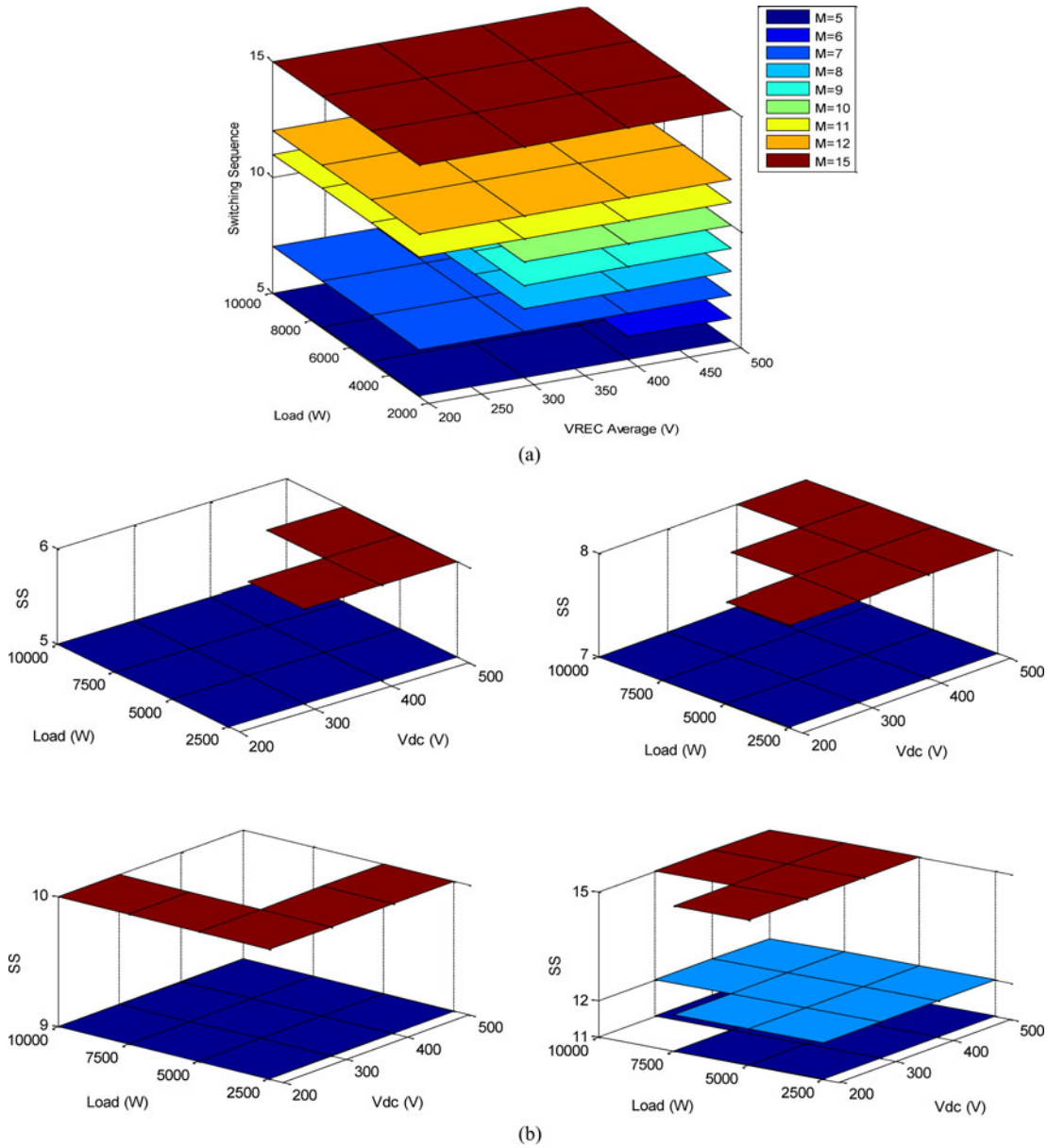

Fig. 6 (a). Plot showing the stability / reachability of switching sequences in Table III for the HFL inverter versus the input voltage dc component (a_0) and load power. Existence of a plain (associated with a specific switching sequence according to the legend) shows the reachability of that specific switching sequence, whereas the extents of the plain show the range of load power and input voltage dc component for which the switching sequence is reachable. It is shown that the switching sequences $M = 13$ and 14 are not reachable for any range of a_0 and PL. (b) Plot showing the stability / reachability of switching sequences in Table III for the HFL inverter versus the input voltage dc component (a_0) and injected power into the grid. Existence of a plain (associated with a specific switching sequence according to the z-axis) shows the reachability of that specific switching sequence whereas the extents of the plain show the range of injected power into the grid and input voltage dc component for which the switching sequence is reachable. It is shown that the switching sequences $M = 13$ and 14 are not reachable for any range of a_0 and PG.

switching state, as follows:

$$X\left(t_0 + T_w\right) = f(X\left(t_0\right), \alpha_i, T_w, A, \{B_i\}_{i=1,\ldots,h}) \qquad (19)$$

where the function $f(.)$ depends on the dynamics of the HFL inverter over the time horizon T_w. The last step is to determine the optimal time horizon (T_w), the optimal switching sequence, and the optimal duration of time VSI spends in each switching state of that optimal sequence ($\{\alpha_i\}_{i=1,\ldots,h}$). Choice of the cost function is user dependent and may also vary with applications and operating conditions. In this paper, cost function will include the output VR or grid control in the single-objective optimization and VR or grid control and switching-loss reduction (SLR) in the multiobjective optimization problem. The constraints for the optimal control problem include the map (19) and the maximum values that each state can attain ($X_{\max}$). The SROC optimization

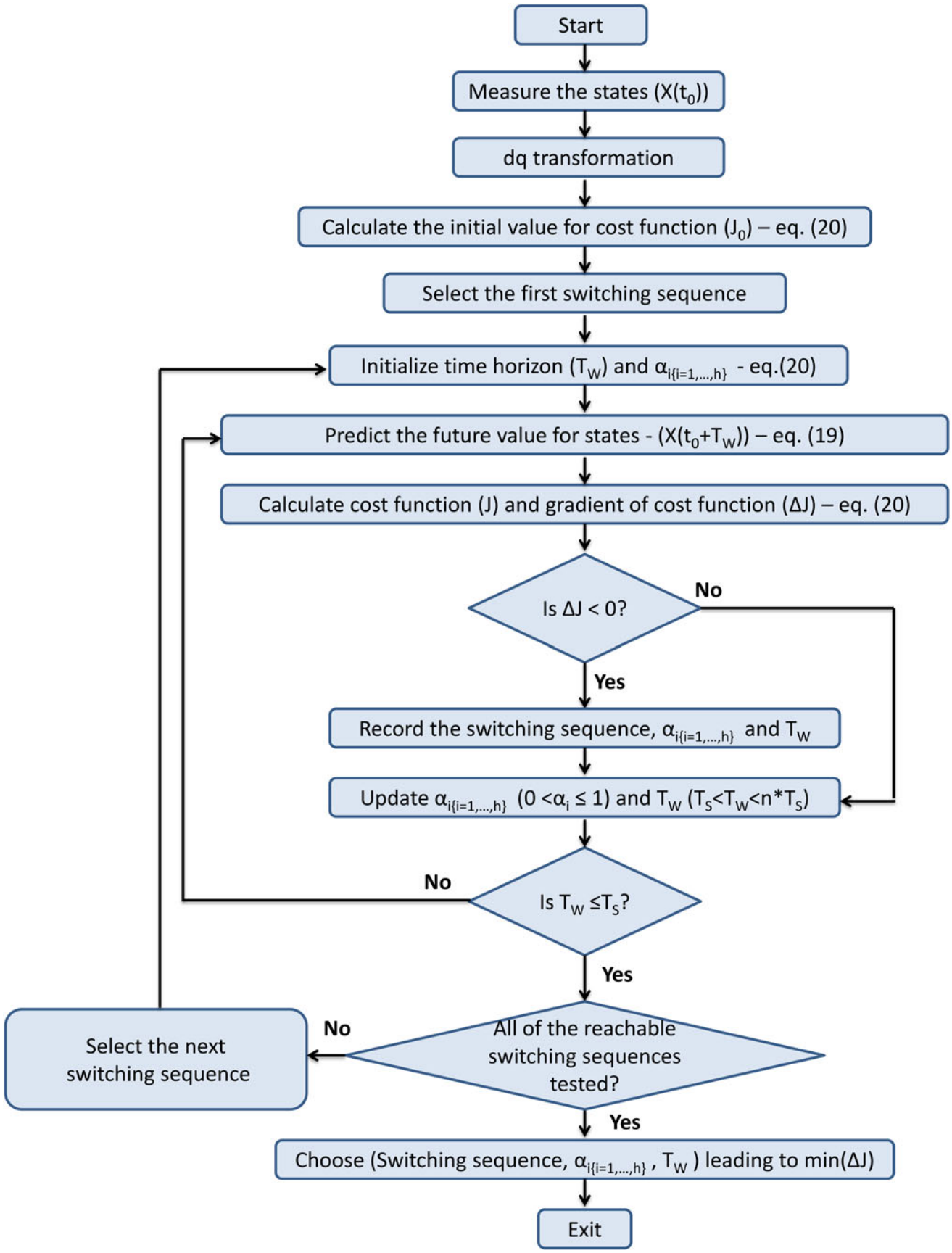

Fig. 7. Flowchart of implementation of OSBC in DSP.

problem can be summarized as to determine $\{\alpha_i\}_{i=1,\ldots,h}$ and T_w that minimizes the cost function $J(.)$.

$J(\{\propto_i\}_{i=1-h}, T_w) = (x^* - x(t_0+T_w))^T P(x^* - x(t_0+T_w))$ given the constraints $x(t_0+T_w) = f(.)$, $x(t_0+T_w) \leq X_{\max}$

$$\sum_{i=1}^{h} \alpha_i = 1 \text{ and } 0 < \alpha_i \leq 1. \tag{20}$$

In (20), P is a positive-definite diagonal matrix and x^* represents the reference values for all of the HFL inverter states. Note that (20) is a quadratic programming problem that can be solved numerically using the conventional algorithms. Whenever $T_w < T_s$, control transitions to the USROC in which $T_w = T_s$ and only $\{\alpha_i\}_{i=1,\ldots,h}$ have to be computed.

Fig. 7 shows a flowchart as used for the implementation of OSBC in a digital processor. Note that J_0 is the initial value of the cost function and T_s is the switching period. In order to implement the OSBC algorithm, many parameters should be taken into consideration such as the processor speed, the total number of parameters to be sensed, the maximum allowable limit for the time horizon, the size of the search space, and the maximum number of iterations to achieve the optimal/suboptimal response. It is obvious that for OSBC, unlike MPC, initially a reachability analysis is conducted to *reduce* the switching-sequence search space to only those switching sequences that ensure reachability. Therefore, the execution time of the OSBC algorithm is reduced and more importantly optimality is ensured under stability bound.

III. Results and Analysis

In this section, first a single-objective optimization problem is considered for VR and grid control using the HFL inverter operating in standalone and grid-connected modes, respectively. Results are compared with those obtained using the conventional linear controller. In the next part, a dual-objective optimization problem is presented that simultaneously regulates the output voltages of the HFL inverter/injected current into the grid and reduces the switching losses by adjusting the switching frequency. MATLAB / Simulink software is used to generate the simulation results presented in this section.

A. Single-Objective OSBC: Standalone Operation

As tabulated in Table IV, 6-kW three-phase resistive load is considered and the nominalswitching frequency of the HFL inverter is assumed to be 40 kHz. Input pulsating-dc voltage source is assumed to have a value of $a_0 = 480$ V and a fundamental frequency of $\omega_0 = 2\pi \times 4 \times 10^4$. The cost function for the single-objective control of the HFL inverter contains weighted terms for $v_d^e = v_d^* - v_d$, $v_q^e = v_q^* - v_q$, and $i_q^e = i_q^* - i_q$ that are d-axis and q-axis voltage error and q-axis current error, respectively. Therefore, the goal of OSBC is to regulate the output voltage of the HFL inverter.

Fig. 8 shows that the d-axis voltage is controlled on the reference value of $v_d^* = 154$ V in almost 50 μs. Fig. 9 shows the same results for v_d and i_d using a linear PI controller. It is shown that the settling time is about 1.6 ms even at a high d-axis proportional gain (K_{pd}) of 2800, which also results in an overshoot of 174 V (about 13%).

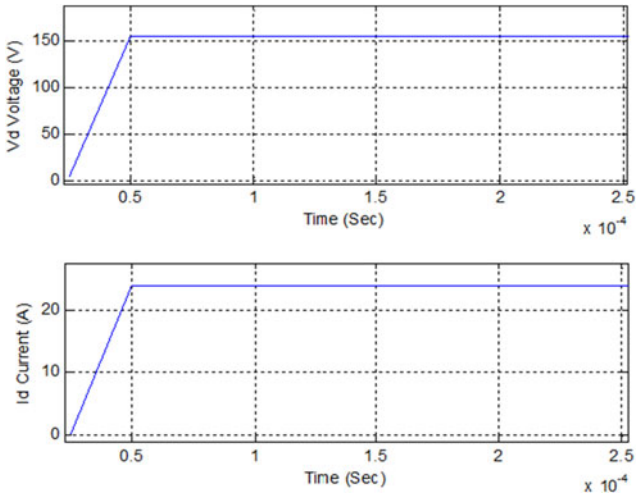

Fig. 8. Single-objective control in standalone operation: VR. Transient response of v_d (top) and i_d (bottom) in a HFL inverter using OSBC. The settling time is found to be 50 μs and no overshoot is observed.

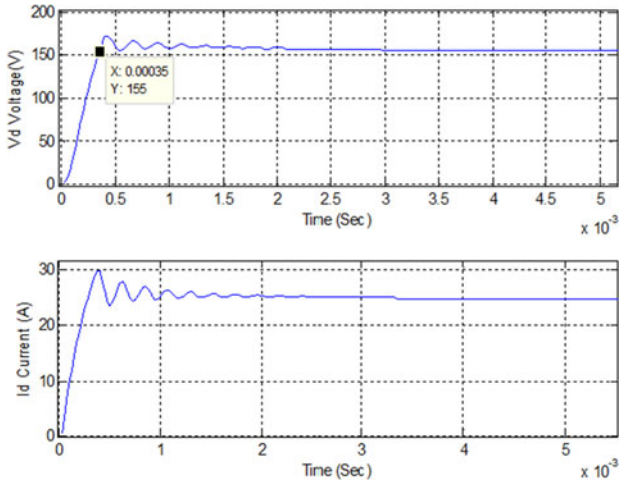

Fig. 9. Transient response of v_d (top) and i_d (bottom) in an HFL inverter using a PI controller for VR ($K_{pd} = 2800$). The settling time is found to be 1.6 ms and an overshoot of 174 V (12.25%) is observed for v_d.

Fig. 10 shows a parametric plot of settling time versus K_{pd} for the PI controller. It is obvious that a compromise has to be made between settling time and overshoot. Even at high gains, still the transient response of the linear controller is a lot slower as compared with the same dynamics obtained using OSBC. Note that in addition, the fast transient response of the OSBC is not achieved for the price of an increase in the overshoot. Moreover, OSBC results in almost no overshoot. Fig. 11 shows the dynamic response of the linear controller to a sudden load change as demanded by the standalone load from the HFL inverter. The pretransient load is supposed to be 3 kW and the posttransient demand is assumed to be 7 kW. A 33% voltage dip is observed

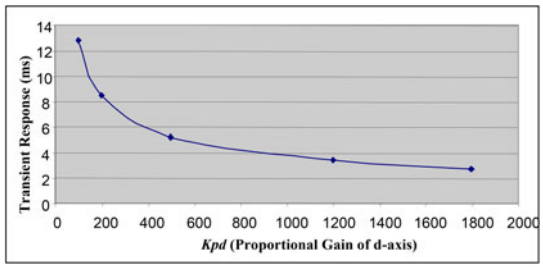

Fig. 10. Parametric plot showing the relationship between the d-axis proportional gain in a linear controller and the settling time of v_d.

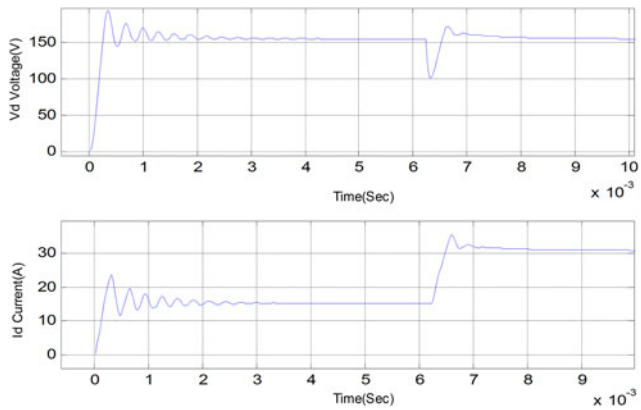

Fig. 11. Dynamic response of the linear controller in a sudden load change at $t = 6.3$ ms from 3.5 to 7 kW in terms of (a) v_d and (b) i_d. A 33% voltage dip is observed and it takes about 2 ms for the controller to adjust voltage and current to the set points.

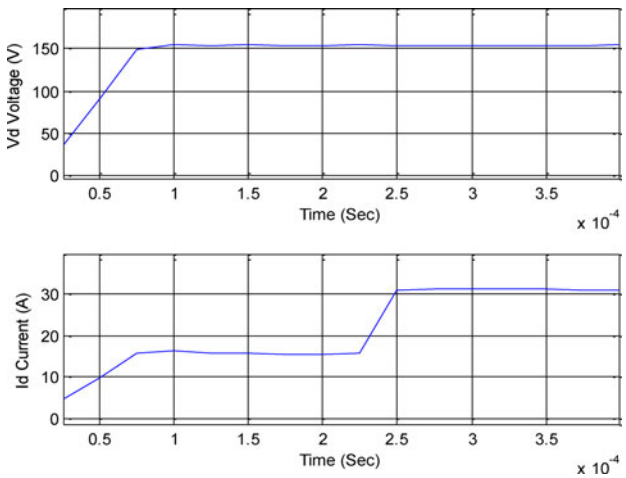

Fig. 12. Dynamic response of OSBC in a sudden load change at $t = 225$ μs from 3.5 to 7 kW in terms of (a) v_d and (b) i_d. Almost no voltage dip is observed and it takes only 25 μs for the controller to adjust voltage and current to the set points.

and it takes about 2 ms for the controller to adjust the voltage and current to the set points. However, in Fig. 12, it is shown that the OSBC can almost seamlessly respond to this load demand in about 25 μs and almost no voltage dip is observed. Fig. 13 shows the evolution of switching sequences corresponding to the startup and load change transients (refer to Table III for interpretation of switching sequences). It is observed that at

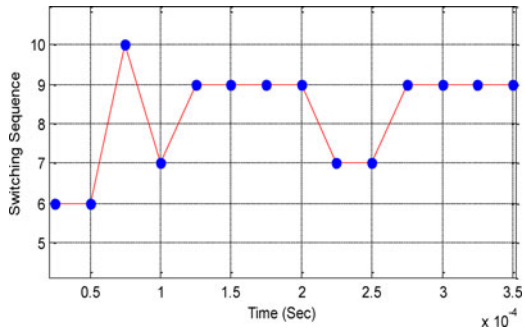

Fig. 13. Evolution of switching sequences corresponding to the startup and load change transients. It is observed that at startup, switching sequences 6,10,7, and 9 are chosen by OSBC, and in 125 μs, steady state is reached through SS $= 9$. At $t = 225$ μs again switching sequence 7 is chosen to remove the transient and adjust the load level to the new set point.

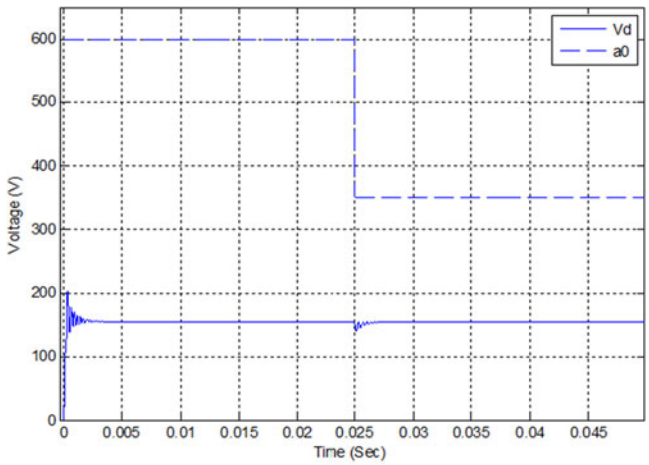

Fig. 14. Transient response of a linear controller (PI) to a sudden change in the dc component of V_{REC} (a_0) in standalone operation.

startup, switching sequences (SS) 6,10,7, and 9 are chosen by OSBC, and in 125 μs, steady state is reached through SS $= 9$. At $t = 225$ μs, again SS 7 is chosen to remove the transient and adjust the load level to the new set point. Superior dynamic response of OSBC as compared with a linear controller can be demonstrated using a sudden change in the dc component of V_{REC} (a_0) as well. Fig. 14 shows the transient response of a PI-based linear controller to a sudden change in a_0, while Fig. 15 shows the same using OSBC.

It can be observed that in contrary with the PI controller, OSBC leads to almost no voltage dip as the dc component of V_{REC} suddenly falls from 600 to 350 V in this case study. Note that the posttransient value of a_0 is in the range of reachability according to Fig. 6. Otherwise, none of the two controllers could stabilize the output voltage of the HFL inverter.

B. *Single-Objective OSBC: Grid-Connected Operation*

In this section, cost function includes the regulation of the PV voltage (V_{DC}) and grid currents according to a predetermined MPPT algorithm (perturb & observe—P&O method). In order to perform grid current regulation and MPPT simultaneously,

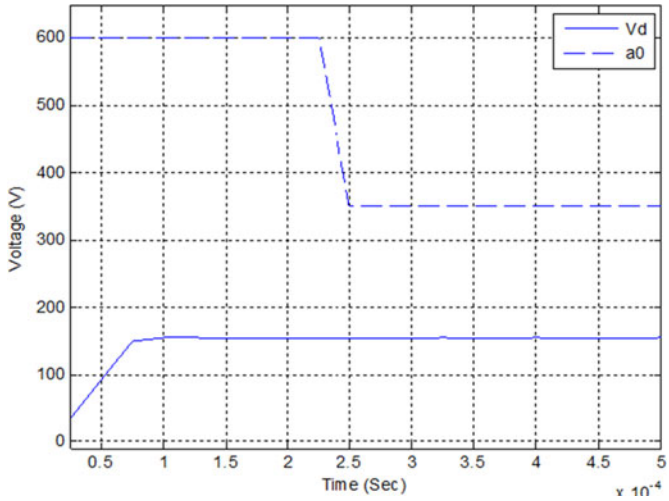

Fig. 15. Transient response of OSBC to a sudden change in the dc component of V_{REC} in standalone operation.

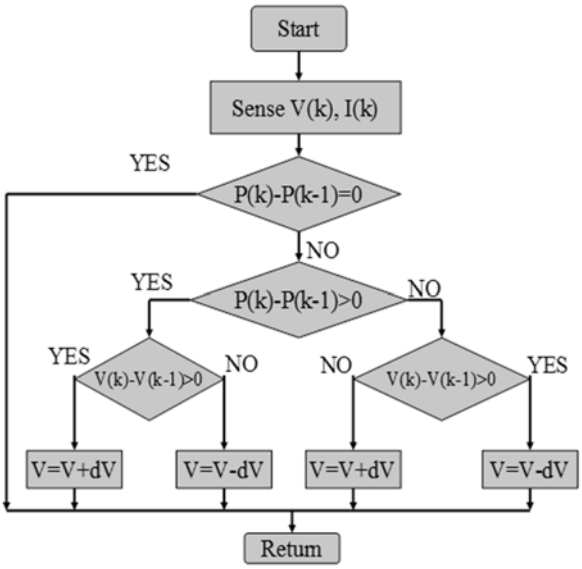

Fig. 16. Sequence of P&O MPPT method.

a cost function is needed with the two terms for regulation of the HFL inverter states in synchronous reference frame (I_d and I_q) as well as the output voltage of the PV array determined by MPPT (V_{DC}) as follows:

$$J = w_1.(I_d^* - I_d)^2 + w_2.(I_q^* - I_q)^2 + w_3.(V_{\mathrm{DC}}^* - V_{DC})^2 \tag{21}$$

where I_d^*, and I_q^* are reference values for the active and reactive currents to be injected to the utility grid and V_{DC}^* is the PV array output voltage determined by the P&O MPPT algorithm, I_d, I_q, and V_{DC} are the measured values for the same and w_1, w_2, and w_3 are weighting factors. In order to extract the maximum power from the PV panels (MPPT), P&O algorithm is incorporated into the optimization process. Fig. 16 shows the flowchart of the P&O algorithm. Fig. 17 shows *I–V* and *P–V* characteristics of the PV array under study. Switching frequency in the unsaturated region

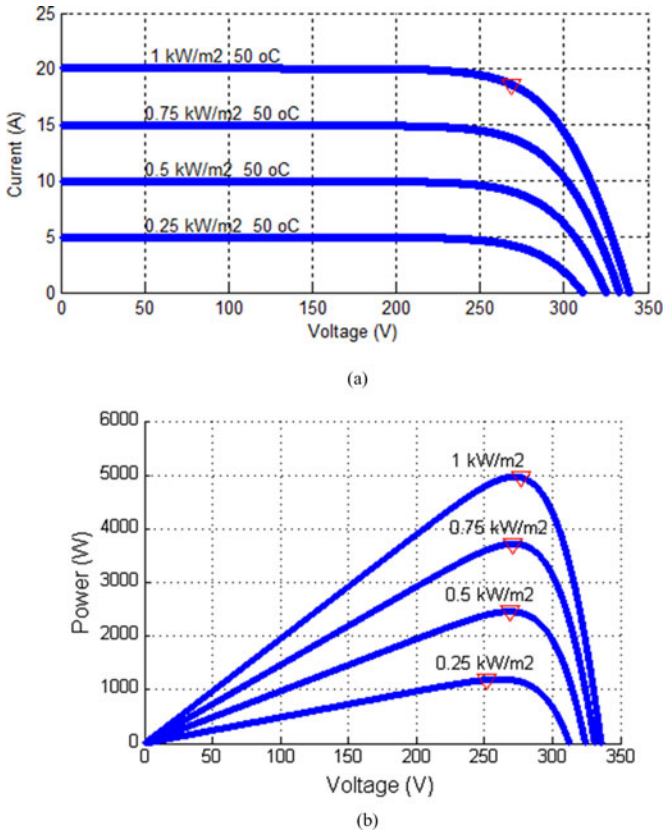

Fig. 17. (a). *I–V* and (b) *P–V* characteristics of the PV array.

is limited to 40 kHz. Output filters are 2 mH per phase and HF transformers turns ratio is 2. In the scenario 1, the irradiance level is assumed to be 1 kW/m^2 and MPPT suggests $i_{\mathrm{pv}} =$ 18 A [see Fig. 17(a)]. Consequently, a value of 277 V for V_{DC}^* is suggested in order to draw the maximum power form PV array. This turns into a value of 4200 W active power to be injected into the grid. Fig. 18 shows the three-phase injected current into the grid in *abc* as well as $\alpha\beta\gamma$ reference frames. Fig. 19 represents the regulation of input dc voltage V_{DC} as a result of inclusion of the third term into the cost function in (21). Fig. 20 demonstrates evolution of the optimal switching sequences from transient to the steady state. In scenario 2, first the irradiance level is 0.5 kW/m^2 and MPPT suggests a value of 260 V for V_{DC}^*. The optimal active power drawn from the PV array is 2350 W and I_d^* is 10 A. At $t = 19$ ms, the irradiance level changes to 0.25 kW/m^2 due to a cloud. Consequently, the reference value for array output voltage (V_{DC}^*) is changed to 250 V leading to optimal active power of 1250 W to be drawn from PV array. The new value for I_d^* is set at 5 A. Fig. 21 shows the regulation of three-phase injected current into the grid in *abc* as well as $\alpha\beta\gamma$ reference frames in response to a sudden change in irradiance level leading to a change in injected active power to maintain the MPPT.

C. Dual-Objective OSBC: Standalone Operation

In this section, a dual-objective cost function is considered in order to optimize both of the VR and SLR goals simultaneously.

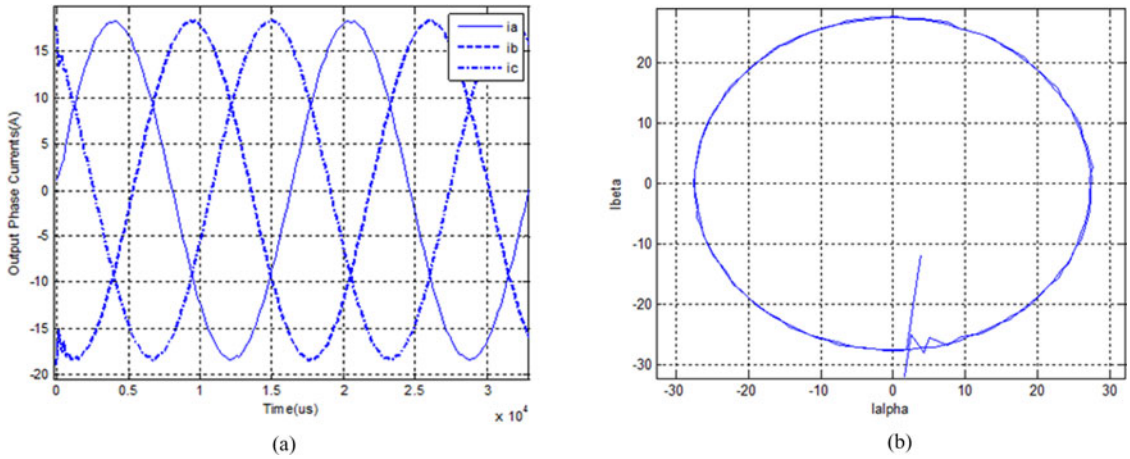

Fig. 18. Control of output injected currents into the grid (a) in *abc* and (b) in $\alpha\beta\gamma$ reference frames using OSBC.

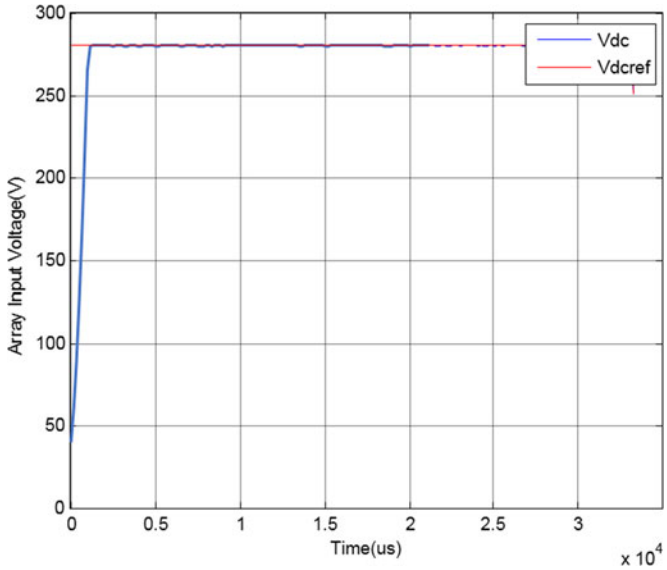

Fig. 19. Regulation of VDC (PV-array voltage) according to the MPPT algorithm.

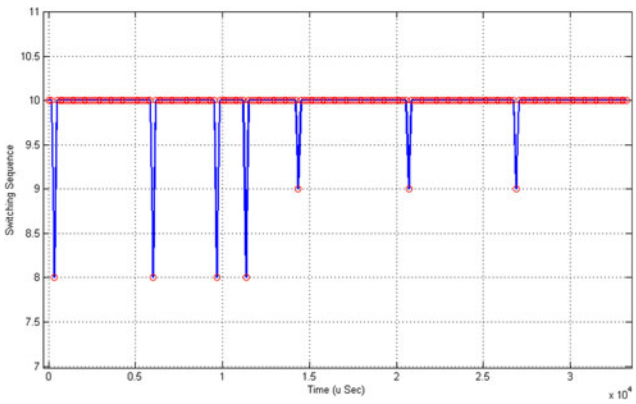

Fig. 20. Evolution of the optimal switching sequences from transient to the steady state.

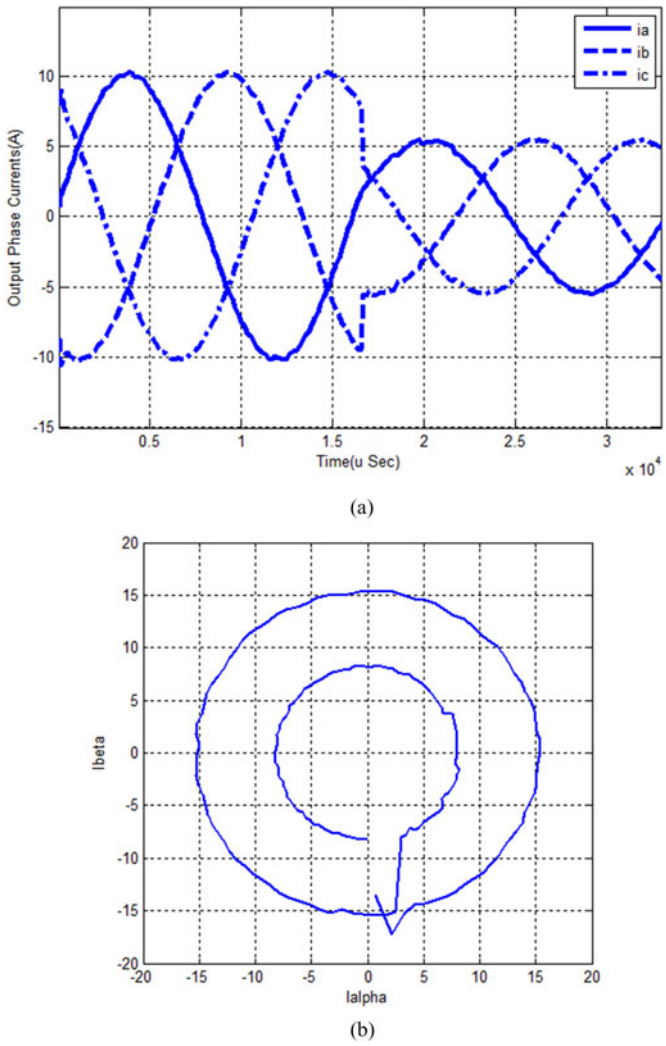

Fig. 21. Control of output injected currents into the grid (a) in *abc* and (b) in $\alpha\beta\gamma$ reference frames using OSBC. Dynamic response to a sudden irradiance level change at $t = 16$ ms.

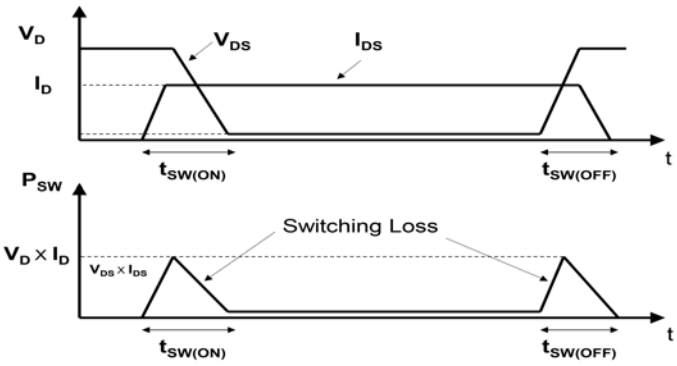

Fig. 22. Illustration of switching loss for a switching device such as a MOSFET.

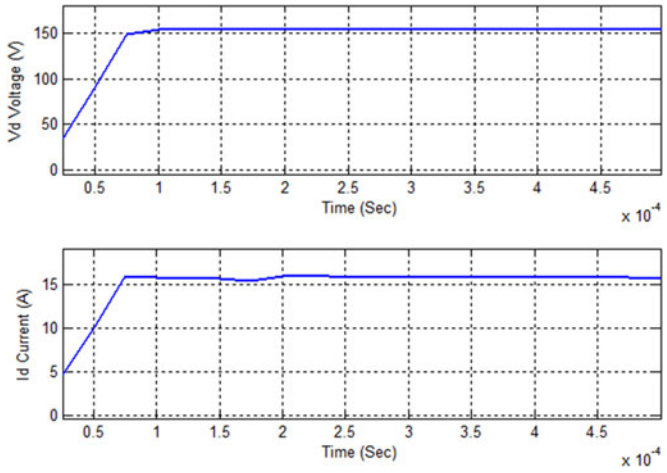

Fig. 23. v_d and I_d in dual-objective (VR and SLR) OSBC for standalone operation.

A 3700-W three-phase resistive load is considered leading to a value of 16 A for I_d and again, $a_0 = 480$ V is considered as the dc component of the pulsating-dc voltage. The cost function for such a multiobjective OSBC is of the form:

$$J = J_{\rm VR} + J_{\rm SLR}, \text{ where } J_{\rm VR} = w_1(v_d^* - v_d)^2 + w_2(v_q^* - v_q)^2 \text{ and } J_{\rm SLR} = w_3 \times \hat{\rm Loss}_{\rm SW} \quad (22)$$

where w_1, w_2, and w_3 are the weighting factors, the first and the second terms represent VR objective, while the third term represents SLR. $\hat{\rm Loss}_{\rm SW}$ is an estimation of switching losses in the AC/AC converter. Generally in an SPC, the switching loss for each switching device (such as a MOSFET) depends on the overlap of the waveforms for the voltage across the drain and the source terminals $v_{\rm DS}$ and the current through the device $i_{\rm DS}$ during the turn-on and turn-off transitions (see Fig. 22) as well as the switching frequency of an SPC. In the HFL inverter of Fig. 1, the total switching loss for the ac/ac converter in one switching cycle can be estimated considering the switching frequency and the area under the $v_{\rm DS} \times i_{\rm DS}$ waveform during the switching transients. The latter depends on the specifications of the semiconductor switch chosen for the SPC as well as the voltage and current ratings for which the SPC is designed. The former, however, inversely depends on the time horizon T_w. In spite of fact that switching frequency somehow is predetermined in the design stage of the HFL inverter filters, isolating HF transformers and in the device selection phase, it can be adjusted in a joint optimization of $\hat{\rm Loss}_{\rm SW}$ along with other cost function terms such as VR in standalone operation as well as current control in grid-connected operation. Regarding what was explained previously and Fig. 22, we have that

$$\hat{\rm Loss}_{\rm SW} = 0.5 \times I_D \times V_D \times (t_{\rm SW(ON)} + t_{\rm SW(OFF)}) \times \left(\frac{1}{T_W}\right) \quad (23)$$

where T_w is the prediction time horizon for OSBC and I_D and V_D are the instantaneous values of device current and voltage.

Fig. 23 shows the d-axis components of output voltage and load current in a dual objective control (VR and SLR) of an HFL inverter operating in standalone mode. Fig. 24 demonstrates the different terms of the cost function associated with the VR at

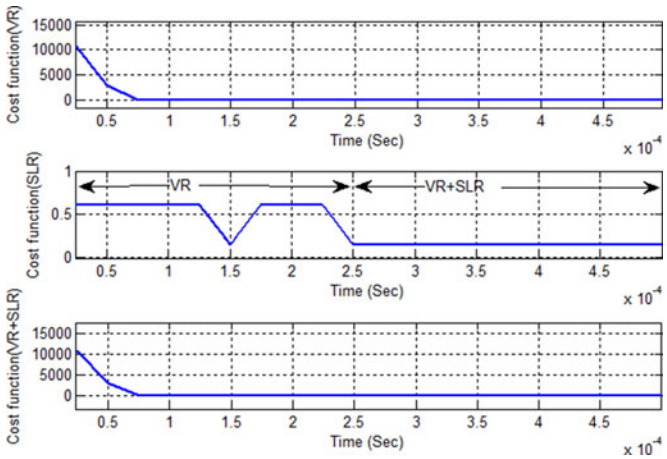

Fig. 24. Cost functions in dual-objective OSBC for standalone operation. Top: cost function of VR ($J_{\rm VR}$), middle: cost function of SLR ($J_{\rm SLR}$), and bottom: total cost function ($J_{\rm VR} + J_{\rm SLR}$).

the top ($J_{\rm VR}$), the SLR goal in the middle ($J_{\rm SLR}$), and the total cost function at the bottom (J). Note that at $t = 250$ μs, the weight of the cost function term for the SLR (w_3) is changed from zero to 0.1 leading to an increase in the switching time period, which reduces the SLR cost function. Also note that the inclusion of the SLR term does not have any adverse effect on VR (see Fig. 23). Fig. 25 shows the evolution of switching sequences during the VR period and the period in which both the VR and SLR goals are included in the cost function to be minimized.

If for a typical MOSFET in the design range of our case study (IXFH 26N60Q), we consider $t_{\rm SW(ON)} = 60$ ns and $t_{\rm SW(OFF)} = 96$ ns (as per datasheet), then for the case illustration shown in Figs. 23 and 24, the amount of SLR per each MOSFET in ac/ac Converter due to dual-objective OSBC would be about 9.75 W (see Table V).

In the grid-connected mode of operation, in a similar way as performed in the standalone mode, HFL inverter can be

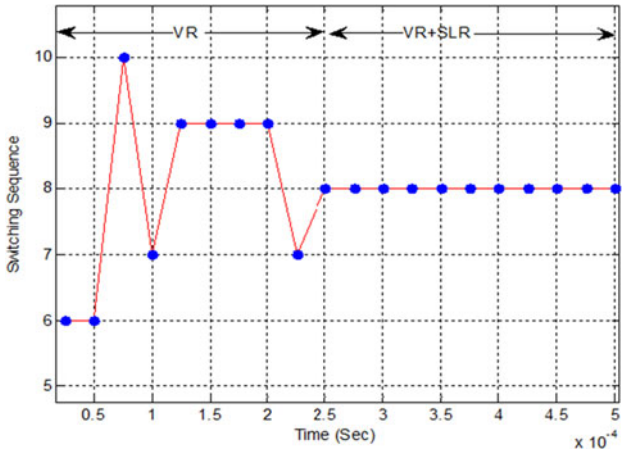

Fig. 25. Evolution of switching sequences in dual-objective control (VR & SLR) of an HFL inverter operating in standalone mode.

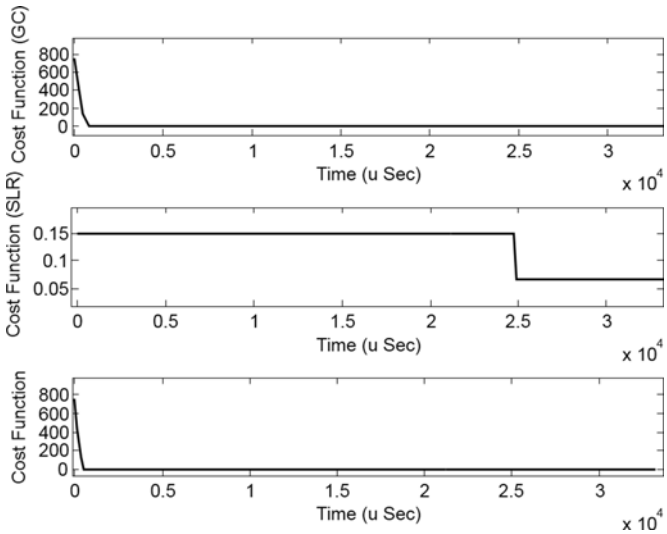

Fig. 26. Cost functions in dual-objective OSBC for grid-connected operation. Top: cost function of GC (J_{GC}), middle: cost function of SLR (J_{SLR}), and bottom: total cost function ($J_{\mathrm{GC}} + J_{\mathrm{SLR}}$).

TABLE IV
SUMMARY OF SIMULATION PARAMETERS

Load type and value	Three-phase resistive load, 6 kW
Input pulsating-dc waveform	DC component: $a_0 = 480$ V, fundamental frequency: $\omega_0 = 2\pi \times 4 \times 10^4$
Cost function for OSBC	$J = w_1.(v_d^* - v_d)^2 + w_2.(v_q^* - v_q)^2 + w_3.(i_q^* - i_q)^2$

TABLE V
SWITCHING LOSS REDUCTION DUE TO DUAL-OBJECTIVE OSBC

Objective function	Weighting factors	Switching frequency	Switching loss per MOSFET
VR	$w_1 = 0.6$, $w_2 = 0.4$, $w_3 = 0$	40 kHz	$\hat{\mathrm{L}}\mathrm{oss}_{\mathrm{SW}_1} = 0.5 \times 600\,\mathrm{V} \times 16\,\mathrm{A} \times 156\,\mathrm{ns} \times 40\,\mathrm{kHz} = 30\,\mathrm{W}$
VR + SLR	$w_1 = 0.5$, $w_2 = 0.4$, $w_3 = 0.1$	27 kHz	$\hat{\mathrm{L}}\mathrm{oss}_{\mathrm{SW}_1} = 0.5 \times 600\,\mathrm{V} \times 16\,\mathrm{A} \times 156\,\mathrm{ns} \times 27\,\mathrm{kHz} = 20.25\,\mathrm{W}$

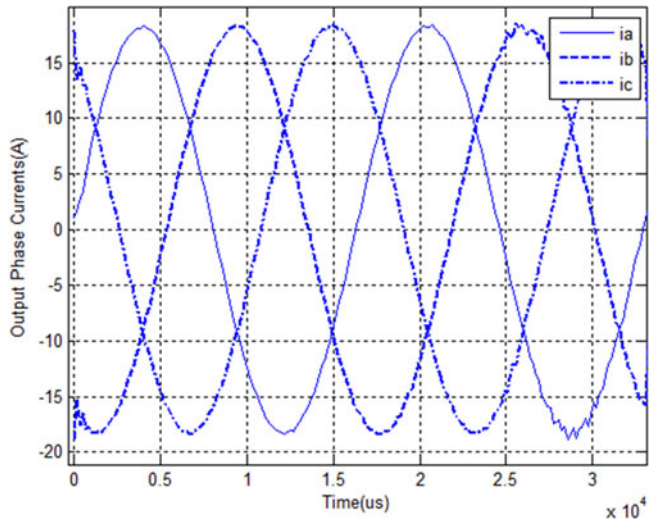

Fig. 27. Control of output injected currents into the grid. Note that inclusion of the SLR term (at $t = 25$ ms) does not have a considerable adverse effect on GC but a little bit of more ripples in injected currents

controlled using multiobjective OSBC. For instance, the injected power to the grid and switching loss reduction could be optimized simultaneously by minimizing the following cost function:

$$J = J_{\mathrm{GC}} + J_{\mathrm{SLR}} \tag{24a}$$

$$J_{\mathrm{GC}} = w_1.(I_d^* - I_d)^2 + w_2.(I_q^* - I_q)^2 + w_3.(V_{\mathrm{DC}}^* - V_{\mathrm{DC}})^2 \text{ and } J_{\mathrm{SLR}} = w_4 \times \hat{\mathrm{L}}\mathrm{oss}_{\mathrm{SW}}. \tag{24b}$$

D. Dual-Objective OSBC: Grid-Connected Operation

Fig. 26 shows the value of individual cost functions (J_{GC} and J_{SLR}) as well as the total cost function versus time. Note that at $t = 25$ ms, the weight of the cost function term for the SLR (w_4) is changed from zero to 0.1 leading to an increase in the switching time period (reduction in the switching frequency from 40 to 27 kHz), which reduces the SLR cost function (reduction of switching losses from 30 to about 20 W per MOSFET). Also note that the inclusion of the SLR term does not have a considerable adverse effect on GC but a little bit of more ripples in injected currents (see Fig. 27).

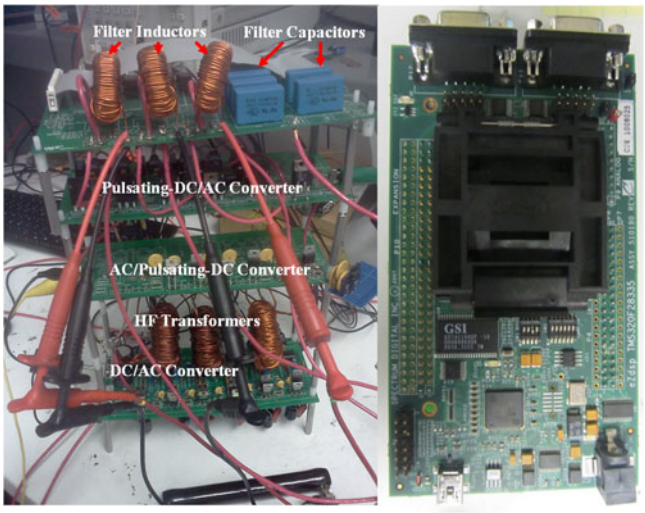

Fig. 28. (Left) 1-kW isolated and multistage HFL inverter prototype developed for validation of the proposed OSBC scheme. (Right) TMS320F28335 DSK board that generates the switching signals.

E. Experimental Implementation Considerations

As stated before, in order to implement the OSBC algorithm several parameters should be taken into consideration such as the processor speed, the total number of parameters to be sensed, the maximum allowable limit for the time horizon, the size of the search space, and the maximum number of iterations to achieve the optimal/suboptimal response.

For the hardware prototyping of the controller, a TMS320 F28335 DSP from Texas Instrument with a 150-MHz clock is used that has an instruction cycle time of about 6.77 ns. For a 40-kHz switching frequency (with a corresponding switching period of 25 μs), 3730 instructions are needed to execute the optimal control. In order to be conservative, 3700 instructions can be assumed that results in a 24.7-μs execution time. This includes the time duration required for sensing the output voltages, analog to digital conversion process, digital filtering and signal conditioning / buffering, and implementation of the optimal control as outlined in the flowchart of Fig. 7.

With a total of 15 fundamental switching sequences (tabulated in Table III), the loop in Fig. 7 should be repeated 15 times. The other two inner loops consist of 100 iterations for α and "n" iterations for T_w (time horizon). If we assume $n = 10$, for each switching sequence, a total number of 1000 iterations is required in the worst case of finding the optimal values for α and T_w. If we consider all of the fundamental switching sequence to do the optimization, this leads to a total number of 15 000 iterations. If for each iteration, a typical of ten instructions is assigned, the total time for execution of the optimal control in each switching cycle would be $150000 \times 6.77\,\text{ns} = 1.0155$ ms, which exceeds the switching period. To reduce the execution time of the OSBC algorithm, some of the aforementioned parameters need to be reduced without appreciably compromising the optimal solution. For instance, instead of sequentially covering the whole range of α ($\in (0, 1]$) with a resolution of 10^{-2} for a switching state, a bisection method can be used that yields a search time that is 7% of the original search time. This is because by using the bisection search method the optimal α is found using n iterations, where n satisfies $\frac{1}{2^n} < 0.01$ yielding $n = 7$. Overall, the main advantage of OSBC over MPC can be explained here having provided the previous discussion. In essence, the main difference between OSBC and MPC is that, MPC controls the switching states while the switching sequences (that may/may not be stability bound) evolve, while OSBC, as outlined in this paper, controls the evolution of optimal feasible (reachable) switching sequences and search space is limited to those feasible switching sequences. For instance, if for the HFL inverter in Fig. 3, the average value of V_{REC} (a_0) varies between 200 and 500 V, the search space is limited to a set of reachable switching sequences for this range as $M \in \{5, 7, 11, 12, 15\}$.

Therefore, the execution time of the OSBC algorithm is reduced to 71.085 μs / (15/5) = 23.7 μs. It is noted that, OSBC can also leverage mutated switching sequences that are synthesized using feasible switching sequences (and hence, stabilizing) and can be used to attain converter performances beyond what can be achieved solely using feasible switching sequences, if needed and as applicable.

Experimental results are obtained using a laboratory prototype (see Fig. 28) with the following specifications: nominal input voltage of 40 V, nominal output voltage of 208 V line to line (RMS), nominal switching frequencies of 20 and 40 kHz for the dc/ac and the pulsating-dc/ac converters, respectively. The rated output power is 1 kW. Table VI summarizes some technical specifications of the developed prototype. Figs. 29 and 30 show the experimental results for the stand-alone mode of operation of an HFL matrix inverter connected to a three-phase variable resistive load. Fig. 29 shows the dynamic response of the linear controller to a sudden load change. The pretransient load is 500 W and the posttransient demand is 1 kW. A 33% voltage dip is observed and it takes about 2 ms for the controller to adjust the voltage and current to the set points. However, in Fig. 30, it is shown that the OSBC can almost seamlessly respond to this load demand and almost no voltage dip is observed.

TABLE VI
PHYSICAL SPECIFICATIONS OF THE INVERTER PROTOTYPE

Input voltage	40 V
Output voltage	208 V
Switching frequency (dc/ac Converter)	20 kHz
Switching frequency (ac/Pulsating-dc, Pulsating-dc/ac Converter)	40 kHz
Rated power	1 kW
Controller board	TMS320F28335 (Texas Instrument)
K_{P} (proportional gain), K_{i} (integral gain)	2800, 280

IV. CONCLUSION

A comprehensive study on the proposed OSBC algorithm for an HFL inverter under standalone as well as grid-connected mode of operation was given that was based on a PWL model of the power stage. In essence, the discontinuous modeling that is a

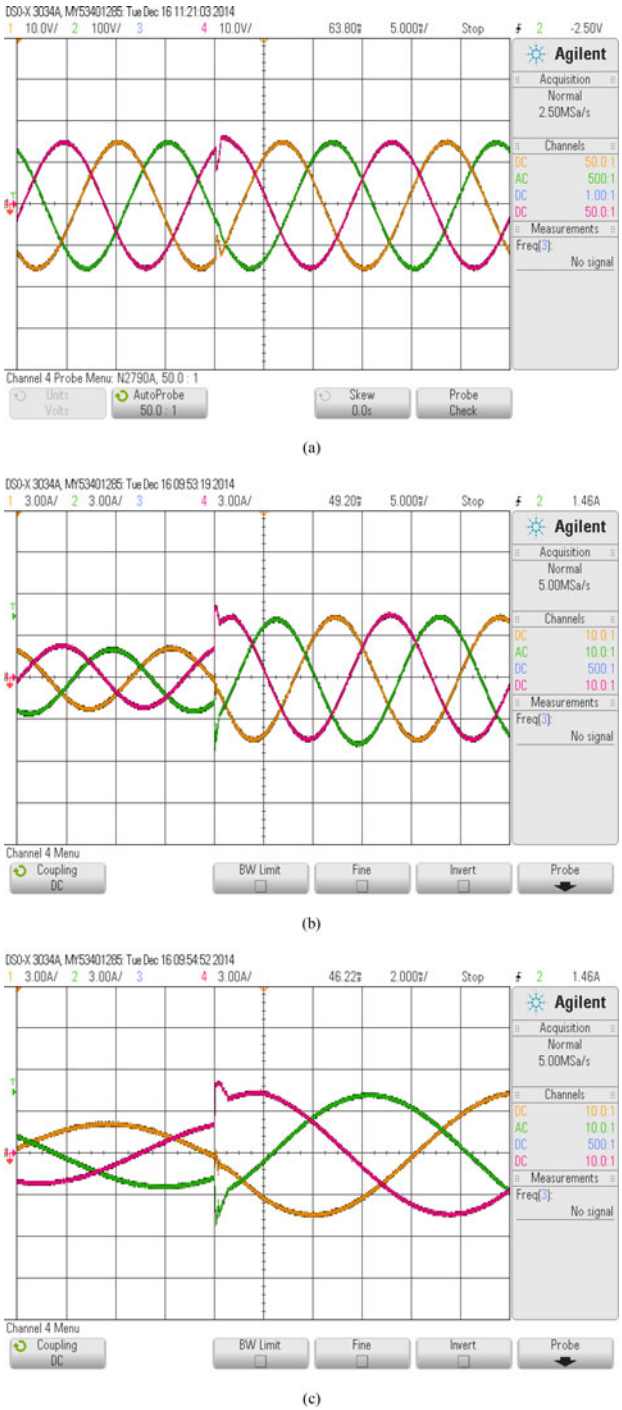

Fig. 29. Dynamic response of the linear controller in a sudden load change from 500 W to 1 kW. (a) Three-phase voltages, (b) three-phase currents, and (c) zoomed version of three-phase currents.

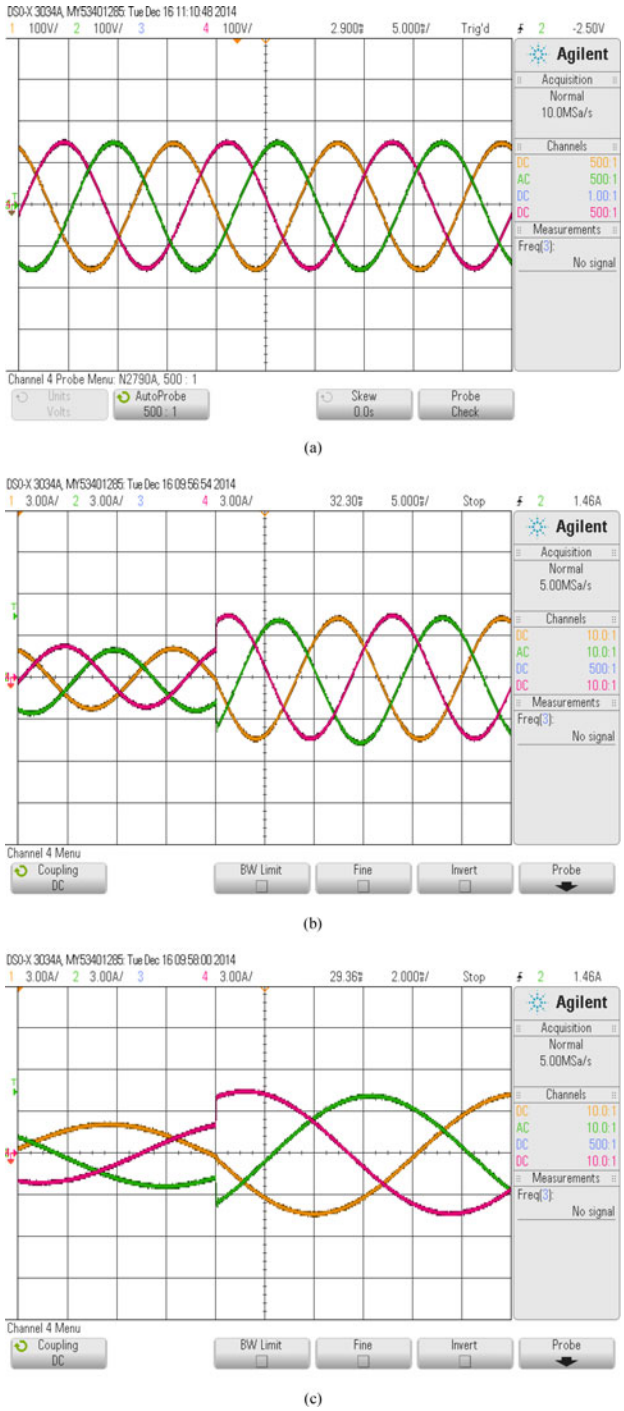

Fig. 30. Dynamic response of the OSBC in a sudden load change from 500 W to 1 kW, (a) Three-phase voltages, (b) three-phase currents, and (c) zoomed version of three-phase currents.

part of OSBC retains both the fast scale as well as the slow scale dynamics, which in turn makes it possible to control multiscale parameters at the same time through a predefined optimization algorithm. The result, as was verified in different parts of this paper, is to attain a superior dynamic response of the OSBC controller as compared with the traditional control approaches that are based on an average model of the power stage. The reason as stated in this paper is the average modeling, which in fact filters the fast scale parameters out.

Another inherent capability of OSBC as verified is the possibility of multiobjective control, which is due to the optimization nature of the OSBC algorithm. This feature is found in the MPC algorithm as well. However, the key difference of OSBC over MPC is restriction of the search space to only reachable switching sequences. This feature enables the OSBC controller

to change the switching sequences as required by the operation mode change of the converter on the fly without any risk of instability. Also, reduction of the search space leads to a reduced execution time for optimal control loops, which in turn increases the controller bandwidth even more. The aforementioned advantages of OSBC for the HFL inverter have been verified through scenario-centric results.

REFERENCES

[1] S. K. Mazumder, J. W. Kolar, H. Akagi, and D. Xu, "Editorial: Special issue on high-frequency-link power-conversion systems," *IEEE Trans. Power Electron.*, vol. 29, no. 8, pp. 3849–3851, Aug. 2014.

[2] S. K. Mazumder, "High-frequency inverters: From photovoltaic, wind, and fuel-cell based renewable- and alternative-energy DER/DG systems to battery-based energy-storage applications," in *Book Chapter in Power Electronics Handbook*, M. H. Rashid, Ed. Burlington, MA, USA: Academic Press, 2010.

[3] D. Grider, M. Das, A. Agarwal, J. Palmour, S. Leslie, J. Ostop, R. Raju, M. Schutten, and A. Hefner, "10 kV/120 A SiC DMOSFET half-bridge power modules for 1 MVA solid state power substation," in *Proc. IEEE Electr. Ship Technol. Symp.*, 2011, pp. 131–134.

[4] L. Empringham, J. W. Kolar, J. Rodriguez, P. W. Wheeler, and J. C. Clare, "Technological issues and industrial application of matrix converters: A review," *IEEE Trans. Ind. Electron.*, vol. 60, no. 10, pp. 4260–4271, Oct. 2013.

[5] M. Amirabadi, A. Balakrishnan, H. A. Toliyat, and W. C. Alexander, "High-frequency ac-link PV inverter," *IEEE Trans. Ind. Electron.*, vol. 61, no. 1, pp. 281–291, Jan. 2014.

[6] K. Basu, R. K. Gupta, S. Nath, and G. F. Castelino, "Research in matrix-converter based three-phase power-electronic transformers," in *Proc. Int. Power Electron. Conf.*, 2010, pp. 2799–2803.

[7] U. R. Prasanna, A. K. Rathore, and S. K. Mazumder, "Novel zero-current switching current-fed half-bridge isolated dc/dc converter for fuel cell based applications," *IEEE Trans. Ind. Appl.*, vol. 49, no. 4, pp. 1658–1668, Jul./Aug. 2013.

[8] T. Mishima and M. Nakaoka, "A load-power adaptive dual pulse modulated current phasor-controlled ZVS high-frequency resonant inverter for induction heating applications," *IEEE Trans. Power Electron.*, vol. 29, no. 8, pp. 3864–3880, Aug. 2014.

[9] T. Besselmann, A. Mester, and D. Dujic, "Power electronic traction transformer: Efficiency improvements under light-load conditions," *IEEE Trans. Power Electron.*, vol. 29, no. 8, pp. 3971–3981, Aug. 2014.

[10] B.-M. Han, N.-S. Choi, and J.-Y. Lee, "New bidirectional intelligent semiconductor transformer for smart grid application," *IEEE Trans. Power Electron.*, vol. 29, no. 8, pp. 4058–4066, Aug. 2014.

[11] A. Rahnamaee and S. K. Mazumder, "A soft-switching modulation scheme for a three-phase capacitor-less pulsating-dc link transformer-isolated inverter," *IEEE Trans. Power Electron.*, vol. 29, no. 8, pp. 3893–3906, 2013.

[12] D. G. Holmes and T. A. Lipo, *Pulse Width Modulation for Power Converters: Principles and Practice*, Hoboken, NJ, USA: Wiley, 2003.

[13] S. K. Mazumder and K. Acharya, "A sequence-based control scheme for voltage-source converters in naval and commercial microgrids," in *Proc. IEEE Electr. Ship Technol. Symp.*, 2009, pp. 461–468.

[14] S. K. Mazumder and K. Acharya, "Multiple Lyapunov function based reaching criteria for orbital existence of switching power converters," *IEEE Trans. Power Electron.*, vol. 23, no. 3, pp. 1449–1471, May 2008.

[15] A. Tajfar and S. K. Mazumder, "A fault-tolerant scheme for an isolated dc/ac matrix converter," *IEEE Trans. Power Electron.*, vol. 30, no. 5, pp. 2798–2813, May 2014.

[16] S. K. Mazumder and T. Geyer. (2014, Aug.). Recent breakthroughs in controls for power electronics. *Proc. Tutorial, Euro. Power Electron. Conf.* [Online]. Available: http://www.epe2014.com/T4%20-%20Mazumder_Geyer_EPE_2014_Tutorial.pdf.

[17] A. Tajfar and S. K. Mazumder, "An optimal sequence-based-controller (OSBC) for a grid-connected three-phase photovoltaic HFL inverter," in *Proc. IEEE Appl. Power Electron. Conf. Expo.*, 2013, pp. 905–911.

[18] A. Tajfar and S. K. Mazumder, "Control of high-frequency-link inverter using optimal switching sequence," in *Proc. IEEE Energy Convers. Conf. Expo.*, 2012, pp. 4703–4710.

Alireza Tajfar (S'10) received the B.Sc. degree in electronics engineering from the Petroleum Institute of Technology, Ahwaz, Iran, in 2002 and the M.Sc. degree in electrical engineering from the Iran University of Science & Technology, Tehran, Iran, in 2005 and the Ph.D. degree in electrical engineering from the University of Illinois, Champaign, IL, USA, in 2014.

He is a Senior Power Electronic Engineer at Enphase Energy, Petaluma, CA, USA, developing high-frequency microinverters used in solar energy applications. He has published more than ten refereed international conference papers. His research interests include power electronics for renewable and alternate energy sources, and modeling, analysis, and control of high-frequency-link power inverters.

Dr. Tajfar is a Reviewer for the IEEE TRANSACTIONS ON POWER ELECTRONICS and the IEEE TRANSACTIONS ON INDUSTRIAL ELECTRONICS and several international conferences.

Sudip K. Mazumder (S'97–M'01–SM'03) received the Ph.D. degree in electrical and computer engineering from Virginia Tech, Blacksburg, VA, USA, in 2001.

He is a Professor in the Department of Electrical and Computer Engineering at the University of Illinois at Chicago (UIC), Chicago, IL, USA. He has 22 years of professional experience and has held R&D and design positions in leading industrial organizations and served as a Consultant for several industries. He has also been the President of NextWatt LLC since 2008.

Since joining UIC, he has been awarded about 40 sponsored projects by leading U.S. federal research organizations and industries. He has published more than 180 journal and conference papers and nine book/book chapters, presented more than 60 invited presentations, and holds eight issued and several pending patents.

Dr. Mazumder serves as the Guest Editor-in-Chief and as an Associate Editor of multiple IEEE Transactions and was the first Editor-in-Chief for *Advances in Power Electronics*. He has served and is serving in high-profile capacities on leading the IEEE Power Electronics Society (PELS) Conference TPCs, PELS TCs, IEEE Working Group, and high-profile NSF panels. He received several prestigious awards including the University of Illinois Chicago's Inventor of the Year Award, University of Illinois' University Scholar Award, IEEE PELS Transaction Prize Paper Award, IEEE Future Energy Challenge Award, ONR Young Investigator Award, and NSF CAREER Award.